Journal of
Applied Remote Sensing

RemoteSensing.SPIEDigitalLibrary.org

Denoising vegetation spectra by combining mathematical-morphology and wavelet-transform-based filters

Xia Zhang
Wenchao Qi
Yi Cen
Honglei Lin
Nan Wang

SPIE.

Xia Zhang, Wenchao Qi, Yi Cen, Honglei Lin, Nan Wang, "Denoising vegetation spectra by combining mathematical-morphology and wavelet-transform-based filters," *J. Appl. Remote Sens.* **13**(1), 016503 (2019), doi: 10.1117/1.JRS.13.016503.

Denoising vegetation spectra by combining mathematical-morphology and wavelet-transform-based filters

Xia Zhang,[a] Wenchao Qi,[a,b,*] Yi Cen,[a] Honglei Lin,[a,b] and Nan Wang[a]
[a]State Key Laboratory of Remote Sensing Science, Institute of Remote Sensing and Digital Earth, Chinese Academy of Sciences, Beijing, China
[b]University of Chinese Academy of Sciences, Beijing, China

Abstract. Spectral noise causes distorted spectra, shifting the central wavelength and thus reducing the accuracy of surface parameter retrieval. A hybrid method combining mathematical-morphology and wavelet-transform (WB)-based filters was used to remove spectral noise. First, a generalized mathematical-morphology (GM) filter was used to remove large-amplitude noise, and then the processed spectra were smoothed using the WT-based filter to remove small-amplitude noise. The simulated noise spectrum and 76 measured canopy spectra for winter wheat were denoised with three filters: the combination filter (CF), GM, and WT. In the simulated experiments, five evaluation indices were calculated to evaluate the denoising effects. For measured spectra, qualitative analyses were performed based on spectral characteristics. Quantitative evaluations were conducted by deriving various vegetation indices from denoised spectra to retrieve wheat's biophysical and biochemical parameters. The results indicated that the CF removed both large- and small-amplitude noise efficiently, improving signal-to-noise ratio and peak signal-to-noise ratio of simulated noise spectrum and retrieval accuracy of leaf water content (LWC) significantly. Meanwhile, it better maintained the waveform and smoothness of spectrum, improving the retrieval accuracies of leaf area index and chlorophyll data slightly. The coefficient of determination (R^2) of developed model between the modified normalized difference water index and LWC was improved from 0.428 to 0.622 using the CF, 0.555 using the GM, and 0.549 using the WT. The R^2 and root mean square error between the measured and retrieval LWC were improved from 0.364 and 0.027 to 0.611 and 0.018 using the CF, whereas the corresponding values were 0.504 and 0.022 for the GM, and 0.478 and 0.023 for the WT. [DOI: 10.1117/1.JRS.13.016503]

Keywords: hyperspectral remote sensing; spectral denoising; mathematical-morphology filter; wavelet-transform-based filter; biophysical and biochemical parameter retrieval.

Paper 180360 received May 1, 2018; accepted for publication Dec. 18, 2018; published online Jan. 11, 2019.

1 Introduction

Hyperspectral remote sensing data provide the advantage of detailed spectral information. However, the spectra of objects are often altered by interference from various noise sources during spectral measurement. Noise in the spectral dimension tends to conceal the true spectral characteristics of ground objects, affecting the accuracy of quantitative applications of hyperspectral images.[1–3] Thus, spectral noise is one of the principal obstacles to further the application of hyperspectral remote sensing data. The need to develop effective methods to eliminate noise interference and recover the intrinsic spectral signatures of objects is urgent and significant. In recent years, several algorithms have been proposed to remove spectral noise. Based on their various background theories, these denoising algorithms can be generally divided into three categories: Savitzky–Golay (SG) filters, wavelet-transform (WT)-based filters, and mathematical-morphology filters.

*Address all correspondence to Wenchao Qi, E-mail: qiwc@radi.ac.cn

Based on the principle of least-squares fitting, SG filters steadily reduce noise using polynomials fitted to the original signal with a small error component.[4–6] Krishnan and Seelamantula[7] applied the SG filter to smooth real-world electrocardiogram signals and addressed the problem of selecting optimal length SG filter. Schettino et al.[8] used an SG filter to detect current-transformer saturation in electrical power system engineering and found that the SG filter removed signal noise and improved the robustness of the detection process. However, the SG filter tended to distort the detailed spectral information.[9]

The WT is a method of localization analysis of time and frequency, which employs a linear combination of wavelet basis functions to represent a signal.[10,11] WTs decompose the input signal into a series of distinctive frequencies that represent different characteristics of the signal and have the capability to reflect the nonstationarity of the signal. With the benefits of multiscale and multiresolution operation, WTs have been widely applied in many studies, including for hyperspectral image denoising,[12,13] compression,[14] classification,[15] and image fusion or enhancement.[16,17] Guo et al.[18] employed a WT filter to the harmonic detection systems. Just once, transform and reconstruction were used to remove a variety of complex noise from harmonic spectrum. Experiments showed that the WT filter could be used for different harmonic detection systems. Rasti et al.[12] used three-dimensional wavelets to remove noise from hyperspectral images, enhancing the spectral features and increasing the accuracy of image classification. Huang et al.[19] used a wavelet threshold denoising algorithm to eliminate the noise of Pound–Drever–Hall signals, further improving the signal-to-noise ratio (SNR) of signal and static-strain measurement resolution. However, selecting the wavelet functions and the decomposition scale of the signal was complicated and difficult.[20,21] In addition, signal drift causes obvious changes in wavelet coefficients,[22] and noise removal using a WT generates pseudo-Gibbs phenomena at the spectrum's endpoints, resulting in signal loss.[23]

Mathematical-morphology filters are a type of nonlinear filters found on set theory. The basic principle of mathematical-morphology filters is that geometric features and correlations between different parts of the signal are extracted with the aid of a structural element, which can be regarded as a probe acting on the signal. Based on purely mathematical foundations and first principles, these filters have been used extensively in the fields of image analysis and signal processing.[24] Li et al.[25] used multiscale morphology for weak microseismic signal detection. Their method decomposed a signal into multiscale components and thus obtained more signal information at selected scales. Dhane et al.[26] performed five filters using mathematical-morphology operations for removing the impulse/random noise from camera-captured digital wound image. The test results demonstrated that the mathematical-morphology filter could obtain higher peak signal-to-noise ratio (PSNR) between the reference original and the filtered image. However, mathematical-morphology filters are unable to remove white noise effectively.[27]

The measured vegetation spectrum usually contains large- and small-amplitude noise, especially in the spectral range of water absorption. Single filter usually does not remove different kinds of noise effectively.[27,28] To remove spectral noise, including small-amplitude noise (such as white noise) and large-amplitude noise (such as pulse noise) effectively, a hybrid method that combines GM filter with WT filter was used to remove noise from spectra in this study. The simulated noise spectrum based on standard vegetation spectrum collected from the United States Geological Survey (USGS) spectral library and the measured canopy spectra of winter wheat were denoised. The performance of the combination filter (CF) was assessed comprehensively through qualitative and quantitative analyses.

2 Materials and Methods

2.1 *Experimental Data*

2.1.1 *Simulated noise spectrum*

One standard vegetation spectrum of grass was collected from USGS spectral library and added with noise in the simulated experiments. The spectrum covers a spectral range of 395 to 2560 nm at spectral resolutions of 2 and 5 nm in the visible and near-infrared spectral range, respectively.

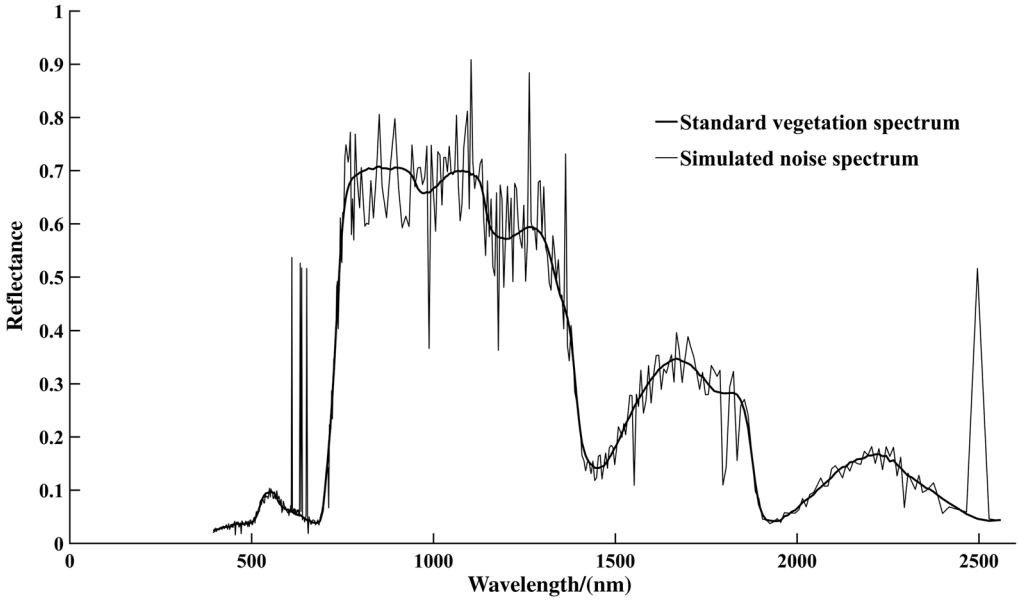

Fig. 1 View of standard vegetation spectrum and simulated noise spectrum.

To obtain simulated spectrum containing large- and small-amplitude noise, the salt-and-pepper noise and multiplicative noise[29] were added to the standard vegetation spectrum together. The standard vegetation spectrum and simulated noise spectrum are shown in Fig. 1.

2.1.2 *Measured canopy spectra of winter wheat*

The canopy spectra of winter wheat and corresponding biophysical and biochemical parameters were used in this experiment. Measurement was conducted in 2001 at Beijing Precision Farming Experimental Station, located in the town of Xiao Tangshan, Changping District, Beijing (40°11′ N, 116°27′E), China.[30] All canopy spectra were measured from a height of 130 cm under clear sky conditions between 10:00 and 14:00 Beijing Local Time. An ASD FieldSpec Pro spectrometer (Analytical Spectral Devices, Boulder, Colorado) fitted with 25-deg field-of-view fiber optics was used to measure the canopy spectra of winter wheat. The spectral range of this spectrometer is from 350 to 2500 nm with sampling intervals of 1.4 nm between 350 and 1050 nm, and 2 nm between 1050 and 2500 nm, and with spectral resolutions of 3 nm at 700 nm and 10 nm at 1400 nm.[31] To reduce the influence of random noise on spectrum, the final spectrum of each sample was determined from the mean of 20 measurements.

Winter wheat samples were obtained immediately after completing wheat spectrum measurements. Then, biophysical and biochemical parameters were determined in the laboratory:[32] wheat leaf water content (LWC) was calculated by drying fresh samples at 60℃ in an oven. Leaf area index (LAI) was calculated using the dry weight method, by drying and weighing 50 to 100 leaves after measuring their leaf areas. Leaf area was then estimated according to the dry weight of leaves and calibrated using a CI-203 laser instrument. Chlorophyll (CHL) concentrations were measured using spectrophotometry. In total, 76 samples and the corresponding biophysical and biochemical parameters were used for the experiment. The specific measurement time and growth stages of wheat are shown in Table 1.

Table 1 Measurement time and corresponding wheat growth stages.

Measure time	April 4	April 14	April 26	May 4	May 13
Growth stages	Erecting	Jointing	Boosting	Heading	Grain filling
Sample numbers	7	18	18	20	13

2.2 *Theory of Mathematical Morphology*

The basic operational steps of mathematical morphology include dilation and erosion, whereas all other operations, such as opening and closing, are derived from these two operations. In addition, diverse combinations of opening and closing operations are used to form the traditional morphology filter and the GM.

Suppose the discrete input signal $f(n)$ is defined as $F = \{0,1, \cdots, N\}$ and the structural element $g(n)$ is defined as $G = \{0,1, \cdots, M\}(\mathrm{N} \geq \mathrm{M})$, then the erosion and dilation operations[33] are defined as follows:

Dilation:

$$(f \oplus g)(n) = \max\{f(n-m) + g(m)\}, \tag{1}$$

Erosion:

$$(f\Theta g)(n) = \min\{f(n+m) - g(m)\}, \tag{2}$$

where $n = \{0,1, \cdots, N-1\}$ and $m = \{0,1, \cdots, M-1\}$.

After determination of both erosion and dilation, the opening and closing operations can be obtained. The opening and closing operations are defined as follows:

Opening:

$$(f \circ g)(n) = [(f\Theta g) \oplus g](n), \tag{3}$$

Closing:

$$(f \bullet g)(n) = [(f \oplus g)\Theta g](n), \tag{4}$$

where $\circ$ stands for the opening operation and $\bullet$ for the closing operation. The erosion and opening operations retain negative impulses and remove positive impulses, and the dilation and closing operations follow the opposite pattern.[34,35] Due to shrinkage of the opening operation, the output amplitude of the opening–closing filter process is small. However, expansion of the closing operation increases the output value of the closing–opening process.[36] To obtain better denoising effects and eliminate the statistical deviation present in a single instance of opening–closing or closing–opening the filter, the following combination is usually adopted:[37]

$$Y(n) = \frac{1}{2}\{F_{\mathrm{OC}}[f(n)] + F_{\mathrm{CO}}[f(n)]\}, \tag{5}$$

where $F_{\mathrm{OC}}[f(n)]$ is the opening and closing filter, with the subscript OC representing an opening operation before a closing operation, and $F_{\mathrm{CO}}[f(n)]$ is the closing and opening filter, with the subscript CO representing an opening operation after a closing operation.

The traditional morphology filter uses a single structural element to remove noise from the signal. However, the denoising effect of a single structural element is limited when there are multiple types and intensities of noise in the signal; therefore, GM filters were proposed.[38] A GM filter is constructed by means of different structural elements, rather than just one kind of structural element, the definitions of which can be expressed as[25]

$$G_{\mathrm{OC}}[f(n)] = f(n) \circ g_1(n) \bullet g_2(n), \tag{6}$$

$$G_{\mathrm{CO}}[f(n)] = f(n) \bullet g_1(n) \circ g_2(n). \tag{7}$$

The average value of these two types of GM filters is thus defined as[39]

$$T(n) = \frac{1}{2}\{G_{\mathrm{OC}}[f(n)] + G_{\mathrm{CO}}[f(n)]\}, \tag{8}$$

where $g_1(n)$ and $g_2(n)$ refer to the different structural elements, $G_{\mathrm{OC}}[f(n)]$ is the opening and closing filter with different structural elements, and $G_{\mathrm{CO}}[f(n)]$ is the closing and opening filter with different structural elements.

2.3 *Theory of the Wavelet-Transform-Based Filter*

If the generating function $\psi(t)$ satisfies Eq. (9) and belongs to $L^2(R)$, which is the space made up of all quadratic integration functions, $\psi(t)$ is called a "base wavelet" or "mother wavelet." The wavelet basis function is a set of function sequences $\{\psi_{a,b}(t)\}$ obtained by calculating the scale and transition of the same mother function

$$C_\psi = \int_{-\infty}^{+\infty} \frac{|\psi(t)|^2}{t} \mathrm{d}t < +\infty. \tag{9}$$

For the continuous case, the wavelet sequence is defined as

$$\psi_{a,b}(t) = \frac{1}{\sqrt{|a|}} \psi\left(\frac{t-b}{a}\right), \tag{10}$$

where $a, b \in R$ and $a \neq 0$, here, a and b are the scaling and translation factors, respectively.

For the discrete case, the parameter a takes the discrete value a_0^j, and the parameter b takes the discrete value $ka_0^j\tau_0$, and thus, the wavelet sequence is defined as

$$\psi_{j,k}(t) = |a_0|^{-j/2} \psi(a_0^{-j}t - k\tau_0). \tag{11}$$

For arbitrary $f(t) \in L^2(R)$, continuous WT is defined as the inner product of the signal $f(t)$ and wavelet function $\psi_{a,b}(t)$, with the specific expansion:

$$W_f(a,b) = \langle f(t), \psi_{a,b}(t) \rangle = \int_{-\infty}^{+\infty} f(t) \frac{1}{\sqrt{|a|}} \overline{\psi}\left(\frac{t-b}{a}\right) \mathrm{d}t, \tag{12}$$

where $a \neq 0$ and $\overline{\psi}_{a,b}(t)$ is a complex conjugate function. In mathematics, the inner product represents the similarity of two functions, and therefore, the above equation can be illustrated as the degree of similarity between $f(t)$ and $\psi_{a,b}(t)$.

For $\psi(t) \in L^2(R)$, where $\psi(t)$ meets the conditions of Eq. (9), and $a = a_0^j$, $b = ka_0^j\tau_0$, then the discrete WT is defined as

$$W_f(j,k) = \langle f(t), \psi_{j,k}(t) \rangle = a_0^{-j/2} \int_{-\infty}^{+\infty} f(t) \psi(a_0^{-j}t - k\tau_0) \mathrm{d}t, \tag{13}$$

if $a_0 = 2$ and $\tau_0 = 1$, then the above equation represents the dyadic discrete WT.

Based on multiresolution analysis, WT decomposes signal into two components, including detail and approximation coefficients.[20] At each scale, the input signal is decomposed by high-pass filters to record high-frequency components and low-pass filters to extract the low-frequency components for the next scale decomposition. For example, as shown in Fig. 2, the signal S was decomposed to four layers, and the signal S can be represented as the sum of CA_4, CD_4, CD_3, CD_2, and CD_1, that is, $S = CA_4 + CD_4 + CD_3 + CD_2 + CD_1$. The CA_1, CA_2, CA_3, and CA_4 are the approximate coefficients that represent the low-frequency components. The CD_1, CD_2, CD_3, and CD_4 are the detail coefficients that represent the high-frequency components.

The signal denoising process based on WT-based filter with soft or hard thresholding is as follows:

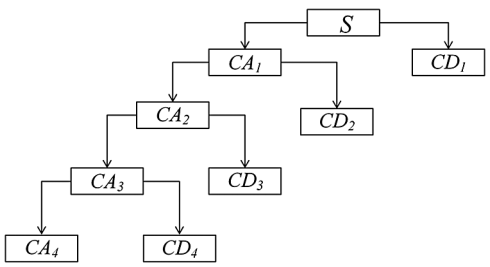

Fig. 2 Schematic diagram of four-layer wavelet decomposition of signal.

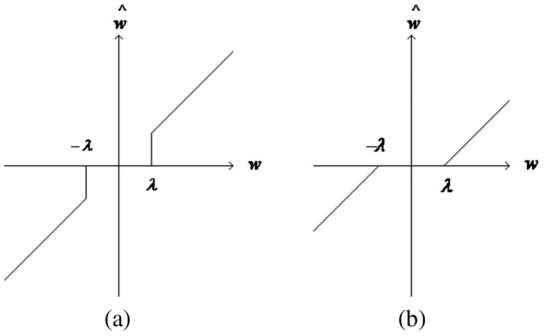

Fig. 3 (a) The hard and (b) soft threshold method to estimate the wavelet coefficients.

i. The signal with noise is decomposed into several layers by multiscale one-dimensional (1-D) wavelet decomposition function, and the approximate and detail coefficients of each layer are extracted successively.

ii. The heuristic threshold selection with soft or hard thresholding was used to set the adaptive threshold for each scale of detail coefficient, including CD_1, CD_2, CD_3, and CD_4. If the SNR is very small, the Stein's unbiased risk estimate is very noisy. If such a situation is detected, the fixed thresholding is used. The soft and hard thresholding are as follows:[40]

Hard threshold estimation:

$$\hat{w}_{j,k} = \begin{cases} w_{j,k}, & |w_{j,k}| \geq \lambda \\ 0, & |w_{j,k}| < \lambda \end{cases}, \tag{14}$$

Soft threshold estimation:

$$\hat{w}_{j,k} = \begin{cases} \text{sign}(w_{j,k}) * (|w_{j,k}| - \lambda), & |w_{j,k}| \geq \lambda \\ 0, & |w_{j,k}| < \lambda \end{cases}, \tag{15}$$

where $\lambda = \partial\sqrt{2\log(N)}$, N is the signal length, and ∂ is the standard deviation of noise (Fig. 3).

iii. Based on the approximate coefficients of the last layer and the detail coefficients of each layer after thresholding, the denoised spectrum is reconstructed by the multiscale 1-D inverse WT.

2.4 *Proposed Method*

As the opening operation can remove positive pulse noise and the closing operation can remove negative pulse noise, the GM filter effectively removes large-amplitude noise from the signal but it has a poor denoising effect on small-amplitude noise.[28,41] The WT uses multiscale analysis of local signal features and enlarges subtle trends, removing small-amplitude noise (such as white noise) effectively. However, when dealing with large-amplitude noise, the WT decomposes partial noise into low-frequency information, and thus the noise is not removed completely.[27] For these reasons, the mathematical-morphology filter and WT were combined for this study. A flowchart of the proposed method is presented in Fig. 4.

The parameter settings have a strong influence on the effectiveness of filter. Previous studies have shown that ball or disk structural elements for mathematical-morphology filters,[42,43] and the Symlet wavelet and Daubechies wavelet methods for WTs, effectively remove noise from the signal.[44,45] In addition, a structural element with a small size can detect detailed signal information but has a weak denoising capacity. Although a large structural element has strong noise-removal ability, it lacks the ability to detect detailed information.[46] The size of the structural element is usually determined according to experimental results and the characteristics of the original signal.[47] In our experiments, ball, disk, diamond, rectangle, and square structural

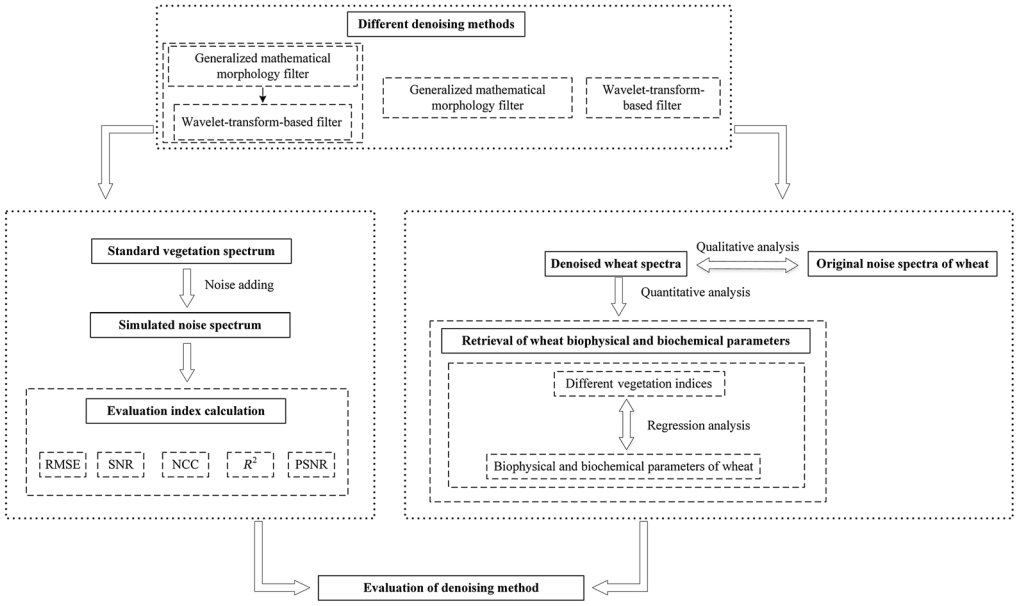

Fig. 4 Flowchart of the proposed method.

elements were used for comparative analysis. In addition, based on the Daubechies wavelet and Symlet wavelet methods, denoising results of the WT with four-layer wavelet decomposition are discussed below.

To evaluate the denoising effects of different filters used in the simulated experiments, five evaluation indices between simulated noise spectrum and standard vegetation spectrum were calculated. To evaluate the application effectiveness of three filters on measured spectra, a subset of 51 canopy reflectance spectra with the corresponding measured biophysical and biochemical parameters were selected randomly from 76 total samples to develop models between vegetation indices and biophysical and biochemical parameters. The remaining 25 samples were used for accuracy validation.

2.5 *Evaluation Criteria*

In the simulated experiments, the normalized correlation coefficient (NCC),[48,49] coefficient of determination (R^2), root mean square error (RMSE), SNR, and PSNR[50] between the smoothed spectrum and standard vegetation spectrum were calculated to evaluate the denoising results. For measured canopy spectra of winter wheat, NCC was used to estimate the waveform similarity of the spectra before and after denoising, to assess the results qualitatively, whereas wheat biophysical and biochemical parameters were retrieved using different hyperspectral vegetation indices derived from denoised spectra to quantitatively assess the results. From seven bands in the visible and near-infrared (VNIR) spectral range and four bands in the shortwave infrared (SWIR) spectral range, seven hyperspectral vegetation indices were calculated. These vegetation indices are commonly used to retrieve biophysical and biochemical parameters. The normalized difference vegetation index (NDVI),[51] structure-insensitive pigment index (SIPI),[52] and modified chlorophyll absorption in reflectance index (MCARI2)[53] were used for retrieval of LAI and CHL. The LWC was retrieved from the normalized difference spectral indices ($NDSI_{1370}$),[54] difference spectral indices (DSI_{1100} and DSI_{1940}),[54] and modified normalized difference water index ($NDWI^*$), which is obtained by multiplying the enhanced vegetation index (EVI) and normalized difference water index ($NDWI_{2500}$).[55–57] Specific definitions of the vegetation indices and evaluation indices used are as follows:

$$\mathrm{NDVI} = \frac{\rho_{800} - \rho_{670}}{\rho_{800} + \rho_{670}}, \tag{16}$$

$$\mathrm{SIPI} = \frac{\rho_{800} - \rho_{445}}{\rho_{800} - \rho_{680}}, \tag{17}$$

$$\mathrm{MCARI2} = \frac{1.5[2.5(\rho_{800} - \rho_{670}) - 1.3(\rho_{800} - \rho_{550})]}{\sqrt{2(\rho_{800} + 1)^2 - \left(6\rho_{800} - 5\sqrt{\rho_{670}}\right) - 0.5}}, \tag{18}$$

$$\mathrm{NDWI}^{*} = \mathrm{EVI} \times \mathrm{NDWI}_{2500}, \tag{19}$$

where EVI is $\frac{2.5\times(\rho_{860}-\rho_{680})}{\rho_{860}+6\times\rho_{680}-7.5\times\rho_{470}-1}$ and NDWI_{2500} is $\frac{\rho_{860}-\rho_{2500}}{\rho_{860}+\rho_{2500}}$.

$$\mathrm{NDSI}_{1370} = \frac{\rho_{1370} - \rho_{2500}}{\rho_{1370} + \rho_{2500}}, \tag{20}$$

$$\mathrm{DSI}_{1100} = \rho_{1100} - \rho_{2500}, \tag{21}$$

$$\mathrm{DSI}_{1940} = \rho_{1940} - \rho_{2500}, \tag{22}$$

where ρ represents the spectral reflectance and its subscript indicates the wavelength (nm). For example, ρ_{800} represents reflectance at a wavelength of 800 nm.

$$\mathrm{SNR} = 10 \times \lg\left[\frac{\sum_{i=1}^{n} f_i^2}{\sum_{i=1}^{n} (f_i - s_i)^2}\right], \tag{23}$$

$$\mathrm{PSNR} = 10 \times \lg\left[\frac{(f_i)_{\max}^2 \times \mathrm{length}(f)}{\sum_{i=1}^{n} (f_i - s_i)^2}\right], \tag{24}$$

$$\mathrm{NCC} = \frac{\sum_{i=1}^{n} s_i f_i}{\sqrt{\left[\sum_{i=1}^{n} s_i^2\right]\left[\sum_{i=1}^{n} f_i^2\right]}}, \tag{25}$$

where s_i and f_i are the wheat spectral reflectance of band i before and after denoising, respectively. They also represent the spectral reflectance of band i for smoothed spectrum and standard vegetation spectrum, respectively. Here, n denotes the band number of spectrum.

$$R^2 = 1 - \frac{\sum_{i=1}^{n} (y_i - x_i)^2}{\sum_{i=1}^{n} (y_i - \overline{y})^2}, \tag{26}$$

where x_i and y_i represent the vegetation index and measured biophysical and biochemical parameters, respectively. They also represent the retrieved and measured biophysical and biochemical parameters, respectively. Here, $\overline{y}$ denotes the mean value of measured wheat biophysical and biochemical parameters.

$$\mathrm{RMSE} = \sqrt{\frac{1}{n}\sum_{i=1}^{n} (y_i - \hat{y}_i)^2}, \tag{27}$$

where y_i and $\hat{y}_i$ represent the measured and retrieved wheat biophysical and biochemical parameters, respectively. They also represent the standard vegetation spectrum and the smoothed spectrum, respectively. Here, n is the number of wheat samples or band number of standard vegetation spectrum.

3 Results and Analysis

3.1 *Experimental Results on Simulated Noise Spectrum*

The simulated spectrum with noise was denoised by different filters. The comparison of denoising effects for different filters is shown in Table 2 and Fig. 5. SNS represents the simulated noise spectrum. WT_1 and WT_4 stand for a WT using three-layer Symlet wavelet function; WT_2 and WT_3 stand for a WT using three-layer Coiflet and Daubechies wavelet function, respectively. GM_1, GM_2, GM_3, and GM_4 stand for a GM using ball-diamond, ball-square, disk-rectangle, and ball-line structural elements, respectively. CF_1 stands for a combination filter using GM_1 and WT_1, and so on.

As shown in Fig. 5, although WT removed small-amplitude noise effectively and the denoised spectra from WT are relatively smooth, the large-amplitude noise was not removed completely. GM removed large-amplitude noise, but the smoothed spectrum showed many broken lines. The denoised spectrum from CF removed both large- and small-amplitude noise, maintaining the waveform and smoothness of spectrum better.

As shown in Table 2, based on the standard vegetation spectrum, the SNR and PSNR calculated using simulated noise spectrum are 13.769 and 19.223 dB, respectively. Moreover, the R^2, RMSE, and NCC are 0.901, 0.077, and 0.979 before denoising, respectively. The NCC and R^2 were improved slightly by the three filters, which demonstrate that the denoised spectrum becomes more similar to standard vegetation spectrum. Compared with GM and WT, the SNR and PSNR calculated using CF were highest, reaching 28.886 and 34.593, respectively, with 25.723 and 31.411 for GM, 21.525 and 27.136 for WT. In addition, the RMSE for CF was lowest with 0.013, whereas RMSE for GM and WT were 0.019 and 0.031. Thus, CF has better denoising ability, improving SNR and PSNR of simulated noise spectrum significantly and maintaining the waveform and smoothness of standard vegetation spectrum in the meantime.

Table 2 Comparison of denoising effects of different filters.

Filter	RMSE	SNR (dB)	NCC	R^2	PSNR (dB)
SNS	0.077	13.769	0.979	0.901	19.223
CF1	0.013	28.886	0.999	0.997	34.593
GM1	0.019	25.723	0.999	0.994	31.411
WT1	0.031	21.525	0.997	0.984	27.136
CF2	0.016	27.184	0.999	0.996	32.833
GM2	0.020	25.167	0.999	0.993	30.806
WT2	0.030	21.736	0.997	0.985	27.351
CF3	0.027	22.867	0.998	0.988	28.460
GM3	0.055	16.691	0.989	0.950	22.163
WT3	0.031	21.619	0.997	0.984	27.232
CF4	0.015	28.066	0.999	0.997	33.771
GM4	0.022	24.421	0.998	0.992	30.098
WT4	0.031	21.525	0.997	0.984	27.136

Note: SNS represents the simulated noise spectrum; WT_1 and WT_4 stand for a WT using three-layer Symlet wavelet function, WT_2 and WT_3 stand for a WT using three-layer Coiflet and Daubechies wavelet function, respectively. GM_1, GM_2, GM_3, and GM_4 stand for a GM using ball-diamond, ball-square, disk-rectangle, and ball-line structural elements, respectively. CF_1 stands for a combination filter using GM_1 and WT_1, and so on.

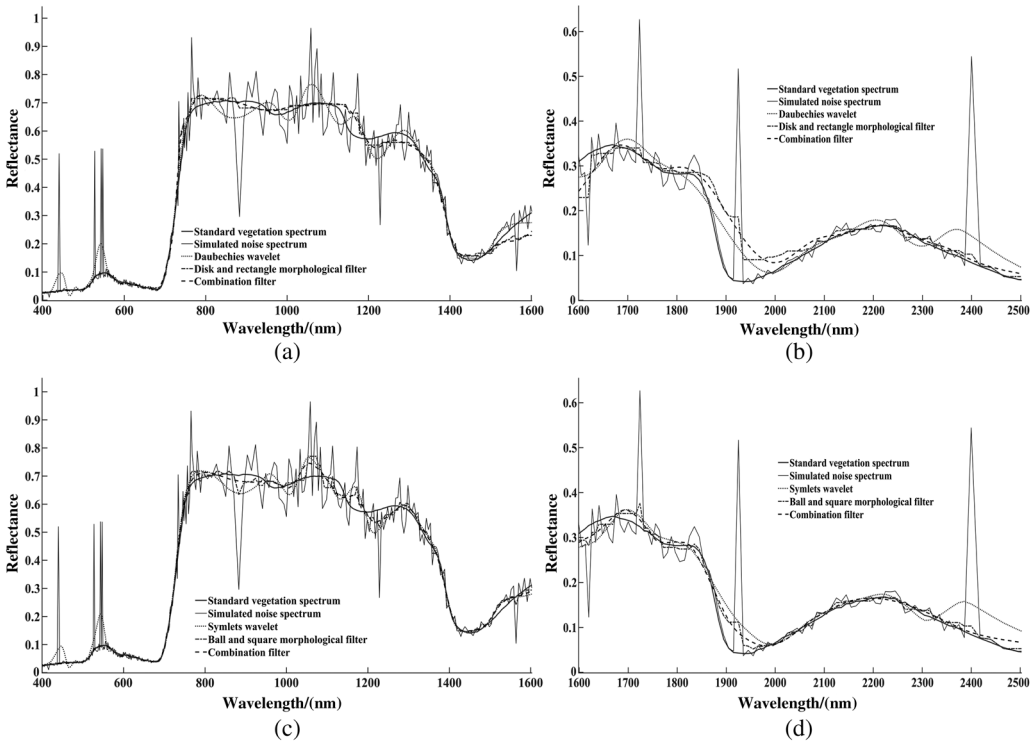

Fig. 5 Local view of spectra with different filters applied: denoising results using Daubechies wavelet with disk-rectangle morphological filter from (a) 400 to 1600 nm, (b) 1600 to 2500 nm, denoising results using Symlet wavelet with ball-square morphological filter from (c) 400 to 1600 nm and (d) 1600 to 2500 nm.

3.2 *Qualitative Analysis of Noise Removal from Measured Spectra*

The sources of spectral noise include variations in light intensity and sensor errors.[58] When incident energy is strongly absorbed by atmospheric water vapor and becomes too weak, the sensor is not able to detect the signal. Thus, field spectra usually contain more noise than spectra measured in the laboratory.[59] The original canopy spectrum (OS) of winter wheat is shown in Fig. 6. This wheat spectrum contains little noise in the VNIR spectral range (400 to 1100 nm) and the spectrum is relatively smooth, as the spectrometer has a high SNR in this spectral range. However, due to the low SNR of the spectrometer and strong water absorption of regions around 1400, 1900, and 2000 nm,[60] the spectrum in the SWIR spectral range (1100 to 2500 nm) contains large-amplitude noise, which appears as "bulges" or "burrs."

Since the OS of winter wheat contains less noise in the VNIR spectral range, NCC values for the CF, GM, and WT are very close to 1 between the original and denoised spectra. For all three filters, the denoised and original spectra overlap in the VNIR spectral range, indicating that none of the filters have a negative influence on the original data in the VNIR spectral range. A comparison of the spectra before and after denoising in different spectral ranges is shown in Fig. 7. Due to the spectra before and after denoising overlay in the VNIR spectral range, to present the result clearly, only the smoothed spectrum from the CF and original spectrum are compared and analyzed in Fig. 7(a). As shown in Fig. 7(a), the smoothed spectrum from the CF and original spectrum almost align within non-noisy spectral regions, reflecting the ability of the CF to maintain spectral signatures. After denoising, the red-edge region (680 to 760 nm) of the wheat spectrum was well preserved. Furthermore, the CF also removed obvious burrs in the form of peaks and valleys in the SWIR spectral range.

Figure 7 shows that all filters could remove large-amplitude noise in the SWIR spectral range, restoring the intrinsic features of original spectrum. However, there were some differences between the denoised spectra obtained using different filters. Compared with the original spectrum, the denoised spectra from the CF and WT are relatively smooth. On the other hand, the denoised spectra from the GM showed many broken lines, especially in the spectral range of

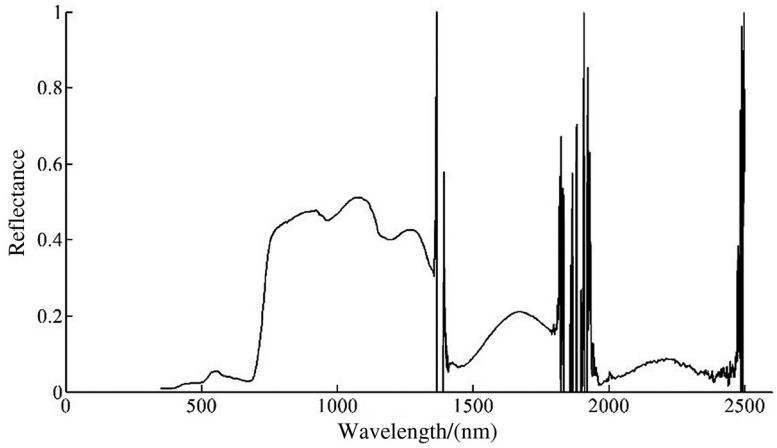

Fig. 6 OS of winter wheat.

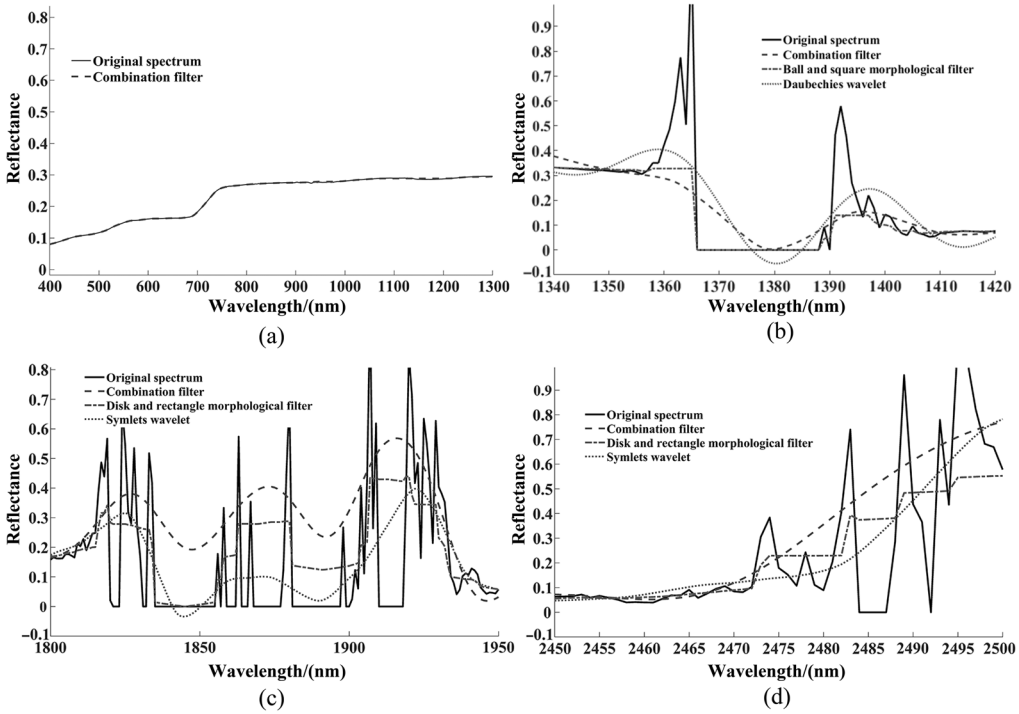

Fig. 7 Local view of spectra with different filters applied: denoising results from (a) 400 to 1300 nm, (b) 1340 to 1420 nm, (c) 1800 to 1950 nm, and (d) 2450 to 2500 nm.

1800 to 1950 nm. The GM with a disk structural element produced more obvious broken lines under various parameter settings. In addition, as shown in Figs. 7(b) and 7(c), the spectral values of the smoothed spectrum obtained using the WT became negative at some wavelengths, which is inconsistent with the measured reflectance spectrum whose values are always positive.

Therefore, although all denoising methods maintained the original spectrum stably in the VNIR spectral range, the CF shows better performance with large-amplitude noise in the SWIR spectral range, removing such noise while maintaining or restoring the spectral shape and value.

3.3 *Quantitative Analysis of Noise Removal from Measured Spectra*

The biophysical and biochemical parameters of winter wheat were retrieved using the denoised spectra. Regression analysis was conducted between the measured and retrieved biophysical and biochemical parameters of winter wheat to verify the denoising accuracy.

Table 3 Accuracy of the models developed between vegetation index, LAI, and CHL using different filters.

	NDVI-LAI	MCARI2-LAI	NDVI-CHL	SIPI-CHL
Filter	R^2	R^2	R^2	R^2
OS	0.5100	0.4390	0.4587	0.3249
CF_4	0.5233	0.4726	0.4801	0.3435
GM_4	0.5103	0.4394	0.4597	0.3248
WT_4	0.5089	0.4370	0.4570	0.3224
CF_5	0.5235	0.4716	0.4800	0.3442
GM_5	0.5100	0.4390	0.4588	0.3249
WT_5	0.5091	0.4373	0.4577	0.3221

Note: OS represents the original spectra; WT_4 and WT_5 stand for a WT using four-layer Daubechies and Symlet wavelet function, respectively. GM_4 and GM_5 stand for a GM using disk-rectangle and ball-square structural elements, respectively. CF_4 stands for a combination filter using GM_4 and WT_4, and so on.

Table 4 Retrieval accuracy of LAI and CHL using different filters.

	LAI (NDVI)		LAI (MCARI2)		CHL (NDVI)		CHL (SIPI)	
Filter	R^2	RMSE	R^2	RMSE	R^2	RMSE	R^2	RMSE
OS	0.6085	0.5920	0.5786	1.4835	0.4663	0.6838	0.3544	0.7799
CF_4	0.6041	0.5977	0.5879	1.4464	0.4790	0.6690	0.3713	0.7572
GM_4	0.6082	0.5924	0.5794	1.4831	0.4669	0.6830	0.3544	0.7799
WT_4	0.6095	0.5913	0.5793	1.4863	0.4657	0.6846	0.3534	0.7788
CF_5	0.6050	0.5969	0.5894	1.4460	0.4793	0.6690	0.3702	0.7595
GM_5	0.6085	0.5922	0.5788	1.4847	0.4664	0.6836	0.3544	0.7799
WT_5	0.6089	0.5917	0.5790	1.4867	0.4658	0.6842	0.3528	0.7768

Note: OS represents the original spectra; WT_4 and WT_5 stand for a WT using four-layer Daubechies and Symlet wavelet function, respectively. GM_4 and GM_5 stand for a GM using disk-rectangle and ball-square structural elements, respectively. CF_4 stands for a combination filter using GM_4 and WT_4, and so on.

The experimental results are listed in Tables 3–6, where different subscripts on the filter names represent different parameters settings. OS means that the original spectra were used to calculate related vegetation indices. GM_4 and GM_5 stand for a GM using disk-rectangle and ball-square structural elements, respectively. WT_4 and WT_5 stand for a WT using the four-layer Daubechies and Symlet wavelet function, respectively. CF_4 stands for a CF using GM_4 with WT_4. CF_5 stands for a CF using GM_5 with WT_5.

3.3.1 *Retrieval of leaf area index and chlorophyll*

Some models of the regression analysis between NDVI and CHL are shown in Table 3 and Fig. 8. The relationships between the retrieved and measured values of CHL are presented in Table 4 and Fig. 9.

Based on regression analysis, NDVI-LAI, MCARI2-LAI, NDVI-CHL, and SIPI-CHL exhibit a significant logarithmic relationship.[61–64] As shown in Fig. 8, the distribution of 51 sample points after denoising was nearly the same as that before denoising. The accuracy of

Table 5 Accuracy of developed model between vegetation index and LWC for different filters.

	NDWI-LWC	DSI_{1100}-LWC	DSI_{1940}-LWC	$NDSI_{1370}$-LWC
Filter	R^2	R^2	R^2	R^2
OS	0.428	0.333	0.266	0.411
CF_4	0.615	0.539	0.486	0.588
GM_4	0.538	0.522	0.448	0.455
WT_4	0.542	0.481	0.444	0.514
CF_5	0.622	0.551	0.506	0.612
GM_5	0.555	0.530	0.502	0.494
WT_5	0.549	0.511	0.500	0.543

Note: OS represents the original spectra; WT_4 and WT_5 stand for a WT using four-layer Daubechies and Symlet wavelet function, respectively. GM_4 and GM_5 stand for a GM using disk-rectangle and ball-square structural elements, respectively. CF_4 stands for a combination filter using GM_4 and WT_4, and so on.

Table 6 Retrieval accuracy of LWC for different filters.

	LWC (NDWI)		LWC (DSI_{1100})		LWC (DSI_{1940})		LWC ($NDSI_{1370}$)	
Filter	R^2	RMSE	R^2	RMSE	R^2	RMSE	R^2	RMSE
OS	0.364	0.027	0.231	0.044	0.214	0.045	0.406	0.026
CF_4	0.610	0.018	0.518	0.021	0.475	0.023	0.640	0.018
GM_4	0.442	0.023	0.343	0.031	0.353	0.030	0.536	0.021
WT_4	0.439	0.024	0.283	0.038	0.267	0.040	0.391	0.025
CF_5	0.611	0.018	0.506	0.021	0.453	0.024	0.625	0.018
GM_5	0.504	0.022	0.387	0.028	0.367	0.029	0.592	0.019
WT_5	0.478	0.023	0.366	0.030	0.392	0.029	0.434	0.023

Note: OS represents the original spectra; WT_4 and WT_5 stand for a WT using four-layer Daubechies and Symlet wavelet function, respectively. GM_4 and GM_5 stand for a GM using disk-rectangle and ball-square structural elements, respectively. CF_4 stands for a combination filter using GM_4 and WT_4, and so on.

the model was not enhanced significantly when using spectra denoised with the generalized morphology or WT, and the R^2 remained basically unchanged from that before denoising. The relationship between retrieved and measured LAI and CHL showed the same pattern. However, for the CF, the accuracy of the developed model was slightly improved. As shown in Table 3, the R^2 of NDVI-LAI, MCARI2-LAI, SIPI-CHL, and NDVI-CHL using denoised spectra from the CF reached 0.5235, 0.4726, 0.3442, and 0.4801, respectively, whereas the corresponding R^2 values were 0.5100, 0.4390, 0.3249, and 0.4587 using the original spectra. The relationship between the retrieved and measured values of biophysical and biochemical parameters was also enhanced, as shown in Table 4 and Fig. 9.

The coefficients of determination between the vegetation indices and biophysical and biochemical parameters remained unchanged or improved slightly, primarily for the following reasons: (1) the bands used in NDVI are in the VNIR spectral range, which is rarely influenced by noise and (2) the CF removed small-amplitude noise in the VNIR spectral range, so the R^2 was slightly improved. This finding shows that the proposed algorithm is capable of removing small-amplitude spectral noise, and thereby restoring spectral information to some extent.

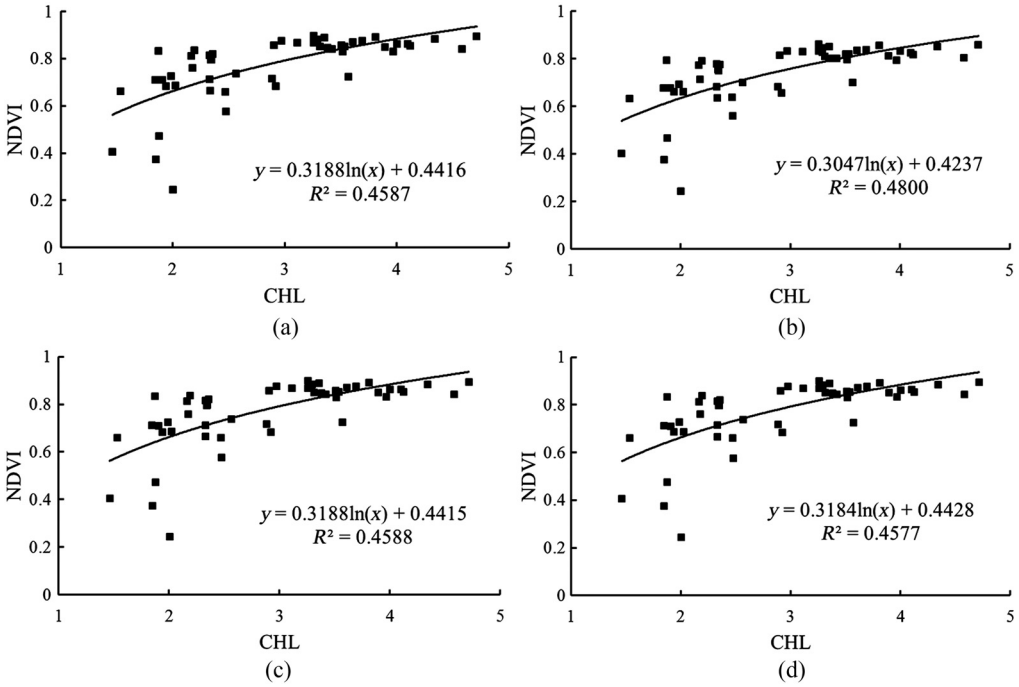

Fig. 8 Model developed between CHL and NDVI: (a) OS of winter wheat, (b) combined filter (CF_5), (c) generalized morphology filter (GM_5), and (d) WT-based filter (WT_5).

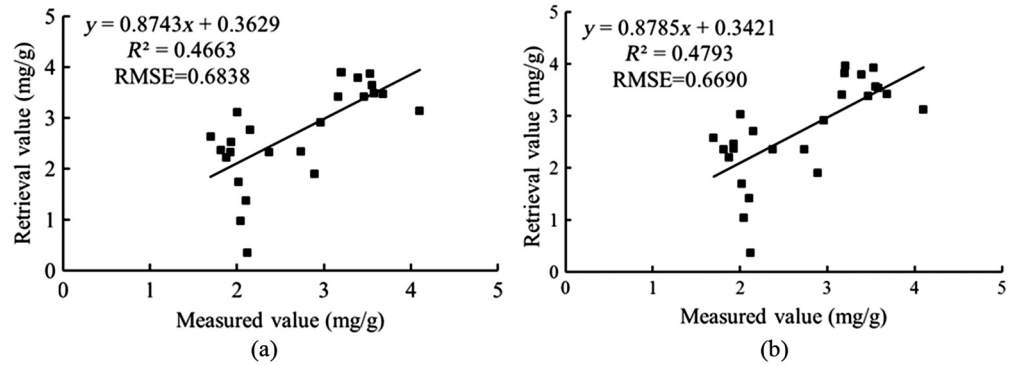

Fig. 9 Measured versus retrieved values of CHL using NDVI: (a) OS of winter wheat and (b) combined filter (CF_5).

3.3.2 *Retrieval of wheat leaf water content*

The specific results of retrieving LWC were listed in Tables 5 and 6. Taking the NDWI* as an example, the regression models were established between NDWI* and LWC, as shown in Fig. 10. Figure 11 shows the LWC retrieval results using NDWI*.

The NDWI* and LWC exhibited a significant logarithmic relationship, as shown in Fig. 10.[65–68] The distribution of sample points after denoising was more concentrated than before. Before denoising, the R^2 between NDWI* and LWC was 0.428. After denoising with three filters, the R^2 reached 0.549, 0.555, and 0.622, corresponding to the WT, GM, and CF, respectively. Among these, the relationship between NDWI* and LWC was most obviously improved after denoising with the CF.

As shown in Fig. 11, there was no strong relationship between retrieved and measured values of LWC before denoising, as the R^2 and RMSE were only 0.364 and 0.027, respectively. After denoising with the three filters, this relationship improved. For the WT, the maximum R^2 value was 0.478 with an RMSE of 0.023. Using the GM, the values of R^2 and RMSE obtained were 0.504 and 0.022, respectively. For the CF, R^2 and RMSE between the retrieved and measured

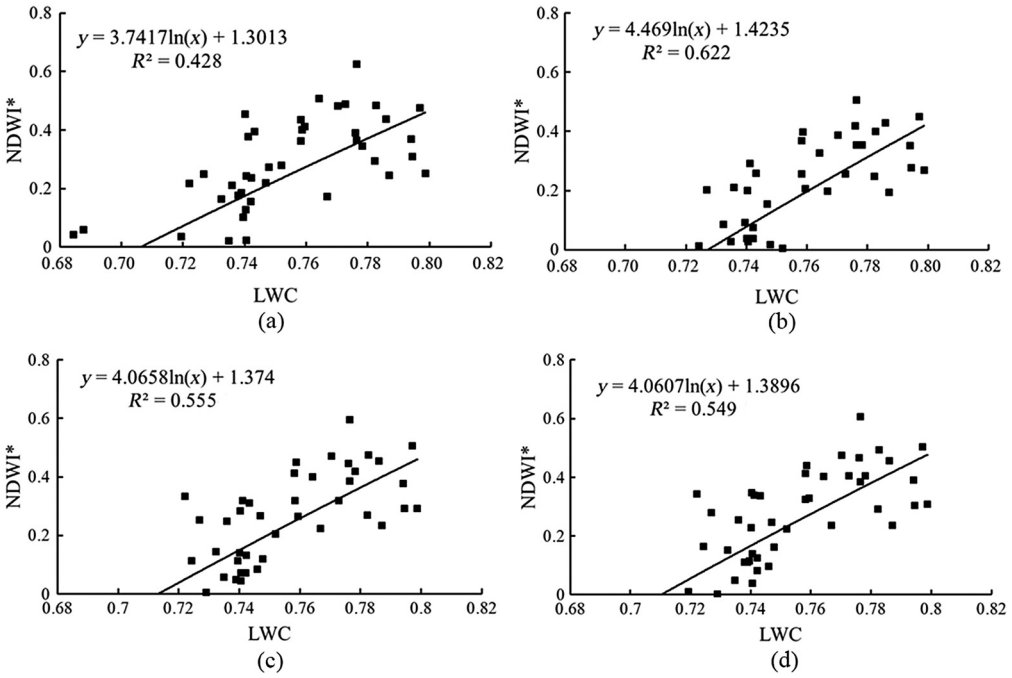

Fig. 10 Model developed between wheat LWC and NDWI*: (a) OS of winter wheat, (b) CF_5, (c) GM_5, and (d) WT_5.

values of LWC were 0.611 and 0.018, respectively, representing a strong improvement over those obtained before denoising. These results show that the regression analysis models obtained using the CF were more reliable than those obtained before denoising and that the CF can provide higher retrieval accuracy for LWC.

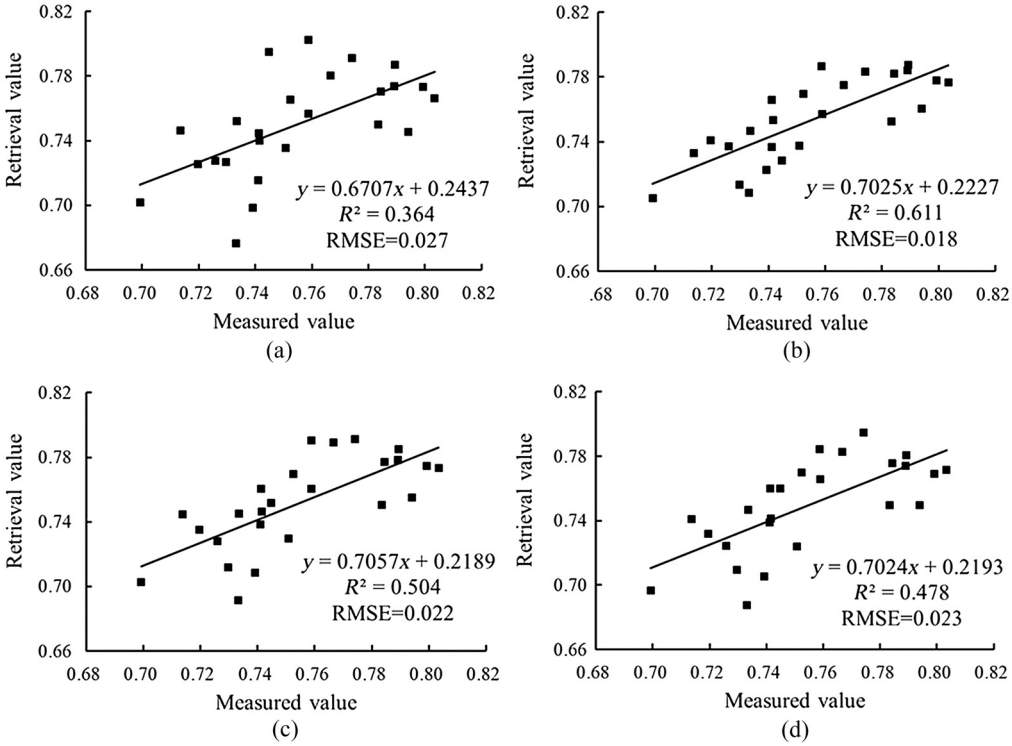

Fig. 11 Measured versus retrieved values of wheat LWC using NDWI*: (a) OS of winter wheat, (b) CF_5, (c) GM_5, and (d) WT_5.

Furthermore, the relationships between LWC and other vegetation indices, including $NDSI_{1370}$, DSI_{1100}, and DSI_{1940}, were also improved after denoising with the CF. The reason for this improvement is that these vegetation indices are calculated mainly using bands in the SWIR spectral range, which contain large-amplitude noise. After denoising with the CF, large-amplitude noise is removed effectively and the spectral characteristics are restored.

4 Discussion

Filtering parameters have a strong influence on the performance of a filter. According to the characteristics of different signals, many experiments have been carried out to select the optimal parameters for the three major filter types. For the mathematical-morphology filter, structural elements are important parameters. Our experimental results show that mathematical-morphology filters with ball, square, rectangular, or disk structural elements can remove large-amplitude noise, but the denoised spectra are distorted to varying degrees, appearing as many broken lines.

Optimization of the WT is focused on selection of wavelet functions and the number of wavelet decomposition layers. Two different wavelet functions, the Daubechies and Symlet wavelet, were used to denoise the wheat canopy spectra. Each wavelet function utilized four-layer wavelet decomposition of the original spectra. As shown in Figs. 12(a) and 12(b), canopy spectra denoised using the WT with certain parameters become negative around 1380 and 1850 nm. This result does not agree with the measured reflectance spectra of winter wheat, which always have values >0. Moreover, this phenomenon is relatively rare in previous research on noise removal from simulated data.[69] This finding also indicates that there are differences between the simulated data and measured field spectra.

The same parameters used with the WT were adopted for the CF. As shown in Figs. 12(c) and 12(d), when the CF was used to remove spectral noise, the denoised spectra were always positive. Also, the spectral curves are smoother than those obtained with the GM, without the appearance of broken lines in denoised spectra. This result shows that the CF enhanced the accuracy of denoised spectra and achieved more effective noise removal.

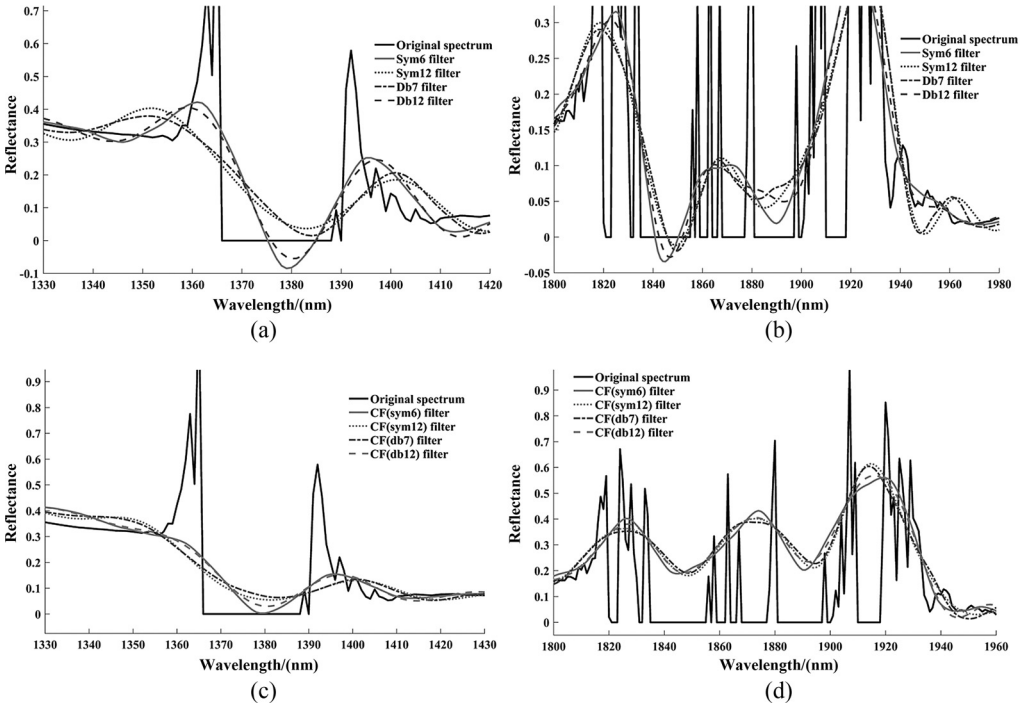

Fig. 12 Local view of spectra obtained using different denoising methods: (a) WT with different parameters from 1330 to 1420 nm, (b) WT with different parameters from 1800 to 1980 nm, (c) CF with different parameters from 1330 to 1430 nm, and (d) CF with different parameters from 1800 to 1960 nm.

No single filter can eliminate noise from a signal completely, particularly in the case of complex noise patterns. However, the CF is able to remove large-amplitude spectral noise in our experiments, which is consistent with previous research. For example, the CF could denoise photoplethysmography signals efficiently, retaining the wave form of the signal well.[22] This filter removes not only large-amplitude noise but also small-amplitude noise.[70] Therefore, it is suitable to apply the CF to removal of spectral noise from winter wheat for restoration of the original spectral characteristics.

5 Conclusion

Spectral noise interferes with the absorption characteristics of objects, limiting the quantitative applications of hyperspectral remote sensing data. A CF was proposed in this study to remove spectral noise. Two commonly used filters, the GM and WT, were used for comparative analysis. The simulated experiments were conducted using simulated spectrum obtained by adding noise to USGS standard vegetation spectrum. Five evaluation indices were calculated to make comparison of different denoising results. Moreover, the measured canopy spectra of winter wheat were denoised by three filters. To evaluate the denoising effects of different filters, regression analysis models were established between vegetation indices and measured biophysical and biochemical parameters. From the viewpoint of practical application of hyperspectral data, the accuracy of the models was validated by retrieving the biophysical and biochemical parameters.

In the simulated experiments, compared with the GM and WT, the CF removed both large- and small-amplitude noise, improving SNR and PSNR of simulated noise spectrum greatly and maintaining the waveform and smoothness of standard vegetation spectrum in the meantime. For measured canopy spectra of winter wheat, the VNIR spectral range (400 to 1100 nm) contained little noise, and all three filters were able to maintain the detailed features of the original spectra. The NCCs in this range were close to 1. In contrast, large-amplitude noise is present in the SWIR spectral range (1100 to 2500 nm). All three filters can suppress large-amplitude noise effectively, confirming their ability to remove spectral noise. However, there are differences between the denoising results of the three filters. The spectra denoised using the GM lack smoothness, exhibiting many twists and turns. Although the WT can produce relatively smooth spectra, negative values present in the denoised spectra are inconsistent with typical vegetation spectra. The CF can remove noise in the SWIR spectral range effectively and exhibits smooth denoised spectra, improving the retrieval accuracy of LWC. Compared with the R^2 of 0.428 before denoising, the R^2 of the model developed between NDWI* and LWC is improved to 0.622 using the CF, to 0.555 with the GM, and to 0.549 with the WT. In addition, the R^2 and RMSE values between retrieved and measured LWC are 0.364 and 0.027, respectively, before denoising, whereas the corresponding values are 0.504 and 0.022 after denoising with the GM, and 0.478 and 0.023 with the WT, respectively. Compared with the GM and WT, the CF obtains the highest retrieval accuracy of LWC, with an R^2 of 0.611 and RMSE of 0.018.

However, this research also identified some shortcomings that must be further explored and addressed. The proposed method focuses on spectral noise removal. Further applications of the CF should be studied and more validation experiments designed. The applicability of this method to other applications, such as hyperspectral image denoising, needs to be confirmed, including whether it might improve the accuracy of spectral unmixing or image classification through spectral noise removal.

Acknowledgments

This work was supported by the National Key R&D Program on Monitoring, Early Warning and Prevention of Major National Disaster (No. 2017YFC1502802), the National Natural Science Foundation of China (No. 41671360), the Central Public Welfare Project (No. 2018SYIAEZD1), and the National Key R&D Program (No. 2016YFB0500502).

References

1. Q. Wang et al., "Low rank constraint and spatial spectral total variation for hyperspectral image mixed denoising," *Signal Process.* **142**, 11–26 (2018).

2. W. Xie and Y. Li, "Hyperspectral imagery denoising by deep learning with trainable nonlinearity function," *IEEE Geosci. Remote Sens. Lett.* **14**(11), 1963–1967 (2017).
3. Y. Chen et al., "Denoising of hyperspectral images using nonconvex low rank matrix approximation," *IEEE Trans. Geosci. Remote Sens.* **55**(9), 5366–5380 (2017).
4. H. L. Kennedy, "Maximally flat IIR smoothers with repeated poles and a prescribed delay," *IEEE Trans. Signal Process.* **64**(19), 4975–4986 (2016).
5. Y. Liu et al., "Applications of Savitzky–Golay filter for seismic random noise reduction," *Acta Geophys.* **64**(1), 101–124 (2016).
6. J.-H. Kim et al., "Performance evaluation of a two-dimensional Savitzky–Golay filter for image smoothing applications," in *Proc. 5th Int. Conf. Electron. Commun. Networks*, A. Hussain, Ed., Springer, Singapore, pp. 309–316 (2016).
7. S. R. Krishnan and C. S. Seelamantula, "On the selection of optimum Savitzky–Golay filters," *IEEE Trans. Signal Process.* **61**(2), 380–391 (2013).
8. B. M. Schettino, C. A. Duque, and P. M. Silveira, "Current-transformer saturation detection using Savitzky–Golay filter," *IEEE Trans. Power Delivery* **31**(3), 1400–1401 (2016).
9. P. J. Curran et al., "Reflectance spectroscopy of fresh whole leaves for the estimation of chemical concentration," *Remote Sens. Environ.* **39**(2), 153–166 (1992).
10. A. S. Antolín and R. A. Zalik, "Some smooth compactly supported tight framelets associated to the quincunx matrix," *J. Math. Anal. Appl.* **437**(1), 35–50 (2016).
11. S. Mallat and W. L. Hwang, "Singularity detection and processing with wavelets," *IEEE Trans. Inf. Theory* **38**(2), 617–643 (1992).
12. B. Rasti et al., "Hyperspectral image denoising using 3D wavelets," in *Int. Conf. Geosci. Remote Sens. Symp.*, pp. 1349–1352 (2012).
13. D. Fang et al., "A sparsity-based InSAR phase denoising algorithm using nonlocal wavelet shrinkage," *Remote Sens.* **8**(10), 830–848 (2016).
14. B. Li, R. H. Jiao, and Y. C. Li, "Fast adaptive wavelet for remote sensing image compression," *J. Comput. Sci. Technol.* **22**(5), 770–778 (2007).
15. X. Huang and L. Zhang, "A multiscale urban complexity index based on 3D wavelet transform for spectral-spatial feature extraction and classification: an evaluation on the 8-channel WorldView-2 imagery," *Int. J. Remote Sens.* **33**(8), 2641–2656 (2012).
16. K. Pyka, "Wavelet-based local contrast enhancement for satellite, aerial and close range images," *Remote Sens.* **9**(1), 25 (2017).
17. N. Han, J. Hu, and W. Zhang, "Multi-spectral and SAR images fusion via Mallat and À trous wavelet transform," in *Int. Conf. Geoinformatics*, pp. 1–4 (2010).
18. Y. Guo et al., "The noise filtering and baseline correction for harmonic spectrum based on wavelet transform," *Spectrosc. Spectral Anal.* **33**(8), 2172–2176 (2013).
19. W. Huang et al., "π-phase-shifted FBG for high-resolution static-strain measurement based on wavelet threshold denoising algorithm," *J. Lightwave Technol.* **32**(22), 4294–4300 (2014).
20. V. D. Hoang, "Wavelet-based spectral analysis," *TrAC Trends Anal. Chem.* **62**, 144–153 (2014).
21. Y. M. Chen et al., "A data-driven threshold for wavelet sliding window denoising in mechanical fault detection," *Sci. China Technol. Sci.* **57**(3), 589–597 (2014).
22. T. Bai et al., "A PPG signal de-noising method based on the DTCWT and the morphological filtering," in *Int. Conf. Signal-Image Technol. Internet-Based Syst.*, pp. 503–506 (2016).
23. H. Z. M. Shafri and P. M. Mather, "Wavelet shrinkage in noise removal of hyperspectral remote sensing data," *Am. J. Appl. Sci.* **2**(7), 1169–1173 (2005).
24. A. Hu and L. Xiang, "An optimal selection method for morphological filter's parameters and its application in bearing fault diagnosis," *J. Mech. Sci. Technol.* **30**(3), 1055–1063 (2016).
25. H. Li et al., "Weak signal detection using multiscale morphology in microseismic monitoring," *J. Appl. Geophys.* **133**, 39–49 (2016).
26. D. M. Dhane et al., "Selection of optimal denoising filter using quality assessment for potentially lethal optical wound images," *Procedia Comput. Sci.* **58**, 438–446 (2015).
27. Y. Chan and X. Miao, "Signal filtering method for early detection of short circuit fault in low voltage power distribution system," *Electr. Eng.* **17**(8), 9–13 (2016).

28. F. Wang and Y. Gan, "Study of traveling-wave singularity detection algorithm based on mathematical morphology," *Electr. Eng.* **16**(4), 26–29 (2015).
29. Z. Chen et al., "Denoising method of spectral signal with multiplicative and additive mixed random noises," *Acta Opt. Sin.* **37**(7), 0730001 (2017).
30. L. Liu et al., "Estimating winter wheat plant water content using red edge parameters," *Int. J. Remote Sens.* **25**(17), 3331–3342 (2004).
31. W. Huang et al., "Managing grain protein content by remote sensing in winter wheat," *Proc. SPIE* **6742**, 67420W (2007).
32. X. Zhang et al., "Study on spectral indices of MODIS for wheat growth monitoring," *J. Image Graphics* **10**(4), 420–424 (2005).
33. J. Serra, "Morphological filtering: an overiew, *Signal Process.*, **38**(1), 3–11 (1994).
34. S. Osman and W. Wang, "A morphological Hilbert–Huang transform technique for bearing fault detection," *IEEE Trans. Instrum. Meas.* **65**(11), 2646–2656 (2016).
35. B. Li et al., "A weighted multi-scale morphological gradient filter for rolling element bearing fault detection," *ISA Trans.* **50**(4), 599–608 (2011).
36. W. Zhang, X. Zhou, and Y. Lin, "Application of morphological filter in pulse noise removing of vibration signal," in *Congr. Image Signal Process.*, pp. 132–135 (2008).
37. X. Mao et al., "Three-dimensional morphological analysis method for geologic bodies and its parallel implementation," *Comput. Geosci.* **96**, 11–22 (2016).
38. J. F. Liu et al., "The noise suppression of magnetotelluric sounding data based on multiple structural elements mathematical morphology filtering," *Geophys. Geochem. Explor.* **38**(1), 109–114 (2014).
39. P. Zhang et al., "Self adjusting composite cascade morphology filter algorithm and its application," *J. Vib. Meas. Diagn.* **35**(3), 459–463 (2015).
40. H. He and Y. Tan, "A novel adaptive wavelet thresholding with identical correlation shrinkage function for ECG noise removal," *Chin. J. Electron.* **27**(3), 507–513 (2018).
41. R. Hu, S. Jiang, and D. Li, "A mathematical morphological filtering approach to remove the noise of MCG-signals," *Mod. Sci. Instrum.* **15**(2), 54–55 (2005).
42. J. Li et al., "Magnetotelluric data processing based on combined generalized morphological filter," *J. Cent. South Univ.* **45**(1), 173–185 (2014).
43. L. Tang et al., "The application of mathematical morphological filtering to the noise suppression of audio magnetotelluric sounding data," *Chin. J. Eng. Geophys.* **42**(11), 33–37 (2013).
44. X. Yang, W. Zhang, and Y. Yang, "Denoising technology of radar life signal based on lifting wavelet transform," *Acta Opt. Sin.* **34**(3), 0328003 (2014).
45. H. Jun and M. You-Liang, "Quantitative study on the selection of wavelet functions for the de-noising of ECG signal," *Inf. Electron. Eng.* **8**(3), 286–289 (2010).
46. F. Wang and L. H. Xia, "Research on application of mathematical morphology in edge detection of high resolution remote sensing image," *Geomatics Spat. Inf. Technol.* **32**(1), 50–53 (2006).
47. L. Hui et al., "Edge detection method of remote sensing images based on mathematical morphology of multi-structure elements," *Chin. Geogr. Sci.* **14**(3), 263–268 (2004).
48. X. Wan et al., "Illumination-invariant image matching for autonomous UAV localisation based on optical sensing," *ISPRS J. Photogramm. Remote Sens.* **119**, 198–213 (2016).
49. G. Bao et al., "Multi-template matching algorithm for cucumber recognition in natural environment," *Comput. Electron. Agric.* **127**, 754–762 (2016).
50. M. F. Zhao et al., "Research on denoising of UV-Vis spectral data for water quality detection with compressed sensing theory based on wavelet transform," *Spectrosc. Spectral Anal.* **38**(3), 844–850 (2018).
51. X. Zhang, W. C. Qi, and W. C. Sun, "Research on vegetation spectrum denoising method based on mathematical morphology filtering," *Remote Sens. Technol. Appl.* **31**(5), 846–854 (2016).
52. L. Liang et al., "Chlorophyll content inversion with hyperspectral technology for wheat canopy based on support vector regression algorithm," *Trans. Chin. Soc. Agric. Eng.* **28**(20), 162–171 (2012).

53. D. Haboudane et al., "Hyperspectral vegetation indices and novel algorithms for predicting green LAI of crop canopies: modeling and validation in the context of precision agriculture," *Remote Sens. Environ.* **90**(3), 337–352 (2004).
54. X. J. Liu et al., "Monitoring leaf water content based on hyperspectra in rice," *Sci. Agric. Sin.* **45**(3), 435–442 (2012).
55. S. Wang et al., "Responses of net primary productivity to phenological dynamics in the Tibetan Plateau, China," *Agric. For. Meteorol.* **232**, 235–246 (2017).
56. Z. Tang et al., "Assessing Nebraska playa wetland inundation status during 1985–2015 using Landsat data and Google Earth Engine," *Environ. Monit. Assess.* **188**(12), 654 (2016).
57. X. J. Cheng et al., "Estimating canopy water content in wheat based on new vegetation water index," *Spectrosc. Spectral Anal.* **34**(12), 3391–3396 (2014).
58. C. Vaiphasa, "Consideration of smoothing techniques for hyperspectral remote sensing," *ISPRS J. Photogramm. Remote Sens.* **60**(2), 91–99 (2006).
59. A. K. Skidmore, "Smoothing vegetation spectra with wavelets," *Int. J. Remote Sens.* **25**(6), 1167–1184 (2004).
60. J. Wang et al., "A wavelet-based area parameter for indirectly estimating copper concentration in Carex leaves from canopy reflectance," *Remote Sens.* **7**(11), 15340–15360 (2015).
61. Z. H. Du, "Study on the scaling and the establishment of the hyper-spectral inversion model of chlorophyll content in rice," China University of Geosciences, Beijing (2015).
62. J. Jiang et al., "Analyzing the spatial scaling bias of rice leaf area index from hyperspectral data using wavelet-fractal technique," *IEEE J. Sel. Top. Appl. Earth Obs. Remote Sens.* **8**(6), 3068–3080 (2015).
63. G. Lin et al., "Retrieving winter wheat leaf area index based on unmanned aerial vehicle hyperspectral remote sensing," *Trans. Chin. Soc. Agric. Eng.* **32**(22), 113–120 (2016).
64. H. L. Jiang et al., "Research on spectral scale effect in the estimation of vegetation leaf chlorophyll content," *Spectrosc. Spectral Anal.* **36**(1), 169–176 (2016).
65. L. Xuan, "Vegetation spectral feature analysis and water content inversion based on hyperspectral remote sensing image," Harbin Institute of Technology (2016).
66. X. Liu et al., "Prediction of moisture content in loess using continuum-removed method," *Wuhan Daxue Xuebao* **42**(5), 661–668 (2017).
67. J. Li, W. Song, and N. F. University, "Water content model for strawberry leaves with spectral signature," *J. Northeast For. Res.* **44**(1), 72–74 (2016).
68. X. Cheng et al., "Inferred water content of winter wheat based on ground hyperspectral and remote sensing data of TM5," *J. Triticeae Crops* **34**(2), 227–233 (2014).
69. W. Zheng et al., "Partial discharge signal obtain based on adaptive wavelet with mathematical morphology," *Phys. Procedia* **24**, 912–917 (2012).
70. H. Li et al., "Research on spectrum denoising methods based on the combination of wavelet package transformation and mathematical morphology," *Spectrosc. Spectral Anal.* **30**(3), 644–648 (2010).

Xia Zhang is a professor at the Institute of Remote Sensing and Digital Earth, Chinese Academy of Sciences (CAS). Her current research interests include hyperspectral image information extraction and classification.

Wenchao Qi is a master at the Institute of Remote Sensing and Digital Earth, CAS. His current research interests include spectral data processing and hyperspectral image classification.

Biographies of the other authors are not available.